

Article

The Characteristics of Submesoscale Eddies near the Coastal Regions of Eastern Japan: Insights from Sentinel-1 Imagery

Gang Li ¹ , Yijun He ^{1,2,*} , Jinghan Wen ³, Guoqiang Liu ^{1,4,5}, Vladimir Kudryavtsev ^{6,7} , Xiaojie Lu ¹ and William Perrie ⁵ 

¹ School of Marine Sciences, Nanjing University of Information Science and Technology, Nanjing 210044, China; cafferylg@gmail.com (G.L.)

² Key Laboratory of Space Ocean Remote Sensing and Applications, Beijing 100081, China

³ Qingdao Joint Institute of Marine Meteorology, Chinese Academy of Meteorological Sciences, Qingdao 266000, China

⁴ Southern Marine Science and Engineering Guangdong Laboratory, Zhuhai 511458, China

⁵ Fisheries and Oceans Canada, Bedford Institute of Oceanography, Dartmouth, NS B2Y 4A2, Canada

⁶ Satellite Oceanography Laboratory, Russian State Hydrometeorological University, St. Petersburg 195196, Russia

⁷ Remote Sensing Department, Marine Hydrophysical Institute, Sebastopol 299011, Russia

* Correspondence: yjhe@nuist.edu.cn

Abstract: A long-term time series of 319 Sentinel-1 SAR Imagery with Interferometric Wide Swath (IW) mode was used to study the characteristics of submesoscale eddies over Japanese coastal regions from 2015 to 2021, including spatiotemporal eddy properties and possible mechanisms of their formation. The results showed that around 98% of the 1499 eddies identified from the SAR snapshots were submesoscale eddies (horizontal scales of $\mathcal{O}(1-20)$ km) with a ratio of around 78% cyclones to around 22% anticyclones. Around 8% of the submesoscale eddies were found in these SAR images in winter since the submesoscale current-induced signals are masked by the stronger wind speed, compared with other seasons. Typical features of submesoscale eddies are summarized, providing a preliminary qualitative analysis of potential generation mechanisms specific to the eddy characteristics in this region. This study suggests that Sentinel-1 images are capable of providing insights into the observed submesoscale eddies near the coastal regions of eastern Japan, thereby contributing to the improved understanding of the generation of submesoscale eddies.

Keywords: submesoscale eddies; Japanese coast; Sentinel-1 imagery with IW mode



Citation: Li, G.; He, Y.; Wen, J.; Liu, G.; Kudryavtsev, V.; Lu, X.; Perrie, W. The Characteristics of Submesoscale Eddies near the Coastal Regions of Eastern Japan: Insights from Sentinel-1 Imagery. *J. Mar. Sci. Eng.* **2024**, *12*, 761. <https://doi.org/10.3390/jmse12050761>

Academic Editor: Eugen Rusu

Received: 11 April 2024

Revised: 28 April 2024

Accepted: 29 April 2024

Published: 30 April 2024



Copyright: © 2024 by the authors. Licensee MDPI, Basel, Switzerland. This article is an open access article distributed under the terms and conditions of the Creative Commons Attribution (CC BY) license (<https://creativecommons.org/licenses/by/4.0/>).

1. Introduction

Oceanic eddies are distributed worldwide in the global ocean and play significant roles in the horizontal and vertical mixing of the upper ocean as well as the transport of energy and marine organisms [1–3]. Submesoscale processes constitute the intermediate scale between large mesoscale processes and small-scale turbulence processes. Therefore, they induce large vertical motions and further enhance vertical mixing, leading to the breakdown of geostrophic balance and energy cascades [4,5]. With horizontal scales of $\mathcal{O}(1-10)$ km and vertical scales of $\mathcal{O}(10-100)$ m, submesoscale eddies are therefore one of the strong ageostrophic processes that also contribute to energy exchange, biogeochemical distributions, and climate change [6–8]. These factors make them a significant consideration for observational and diagnostic analysis. The spatiotemporal analysis of submesoscale eddies near the Japanese coast is currently lacking, which limits our understanding of the oceanic dynamics associated with submesoscale eddies.

Japanese coastal regions, with their numerous capes, turns and islands, are enveloped in wind-driven circulation [9,10] and multiscale processes [11,12]. Submesoscale eddies near the coast have been studied in different regions based on multi-source data [13–16]

and numerical simulation [17,18]. However, the observation of submesoscale eddies along the Japanese coast is limited and lacks systematic analysis. Previous studies on this topic have focused on certain finite regions, such as the Sanriku Confluence of the Tsugaru Warm Current [19], currents of the northwest Pacific Ocean like the Kuroshio water [20], the region off the Sanriku Coast [21], the Kuril Straits [22], the southwestern Japan Sea [23], and the Japanese Coast [24]. These submesoscale eddies have a significant influence on stirring of the tracer gradients and frontogenetic processes.

Synthetic aperture radar (SAR) is a data collection instrument, which can be implemented on satellites/aircrafts, with the advantage of high resolution, wide range, and all-day and all-weather coverage. SAR is, therefore, a good instrument to detect the detailed structures of mesoscale/submesoscale eddies and filaments [25–29], thereby enabling the study of the statistical characteristics and generation mechanisms of submesoscale eddies [30,31]. There are four general mechanisms responsible for eddy manifestations on SAR images: (i) spatial heterogeneity of atmospheric stability due to wind stress over ocean fronts [32], (ii) surface films associated with eddy-induced surface convergence [33,34], (iii) roughness changes caused by wave–current interactions [35], and (iv) spatial redistribution of eddies traced by drifting ice [36]. In SAR images, eddies look like “black” areas at low to moderate wind speeds (~ 0.2 – 5.6 m/s), but appear “white” at higher wind speeds (6 – 12.5 m/s) [32,37].

In this study, a series of Sentinel-1 imagery is used to investigate the structures of submesoscale eddies from 2015 to 2021 near the coastal regions of eastern Japan. The aim is to provide a systematic understanding of the spatiotemporal distribution of the eddies. We further discuss the probable mechanisms of the generation of submesoscale processes associated with background information, such as currents, chlorophyll concentration, and topographic features.

2. Materials and Methods

2.1. Study Area

The Japanese archipelago stretches over 3000 km and has a sea territory of approximately 4,470,000 km² in the Northwest Pacific Ocean. The major axis of the Japanese island system is from southwest to northeast, with a wide southern part narrowing towards the north. The main ocean currents around the Japanese coast are as follows (Figure 1a): (1) First is the Kuroshio Current, which is a strong western boundary current in the northwest Pacific Ocean that plays a critical role in heat transport and circulation exchange [38–40]. To the south of Japan, the Kuroshio enters the deep Shikoku Basin through the Tokara Strait and then encounters the Izu Ridge, in the area known for its bimodal path fluctuations. Large Kuroshio meandering occurs aperiodically from 132° E to 140° E [41], controlled by the interaction between patterns in the Kuroshio path and the magnitude of the Kuroshio’s upstream transport [42]. After separating from the Japanese coast, the Kuroshio Extension is observed as an inertial jet accompanied by large-amplitude meanders and energetic eddies which are pinched off, steered by unstable eddy-driven abyssal mean flows [43]. (2) Second is the Oyashio Current, which is located south of the Bussol Strait, splitting into two paths (the Subarctic Current and the Oyashio intrusion) after passing along the coast of Hokkaido. (3) Third is the Tsushima Warm Current, which constitutes a branch of the North Pacific Subtropical Gyre connecting East China Sea and the East Sea/Sea of Japan [44,45]. (4) Fourth is the Tsugaru Current, which branches from the Tsushima Warm Current and enters the North Pacific Ocean through the Tsugaru Strait. (5) Fifth is the Sōya Warm Current, which is a part of the Tsushima Warm Current, which flows southeastward along the Hokkaido coast, and is a jet-like structure in summer and fall [46]. (6) Sixth is the Liman Current, which is a major current that passes over the trough slope and originates from near the Russian Tatar Strait in the north East Sea/Sea of Japan. The circulation and topographic features of the Japanese coast have been proven to induce mesoscale and submesoscale eddies [47–49].

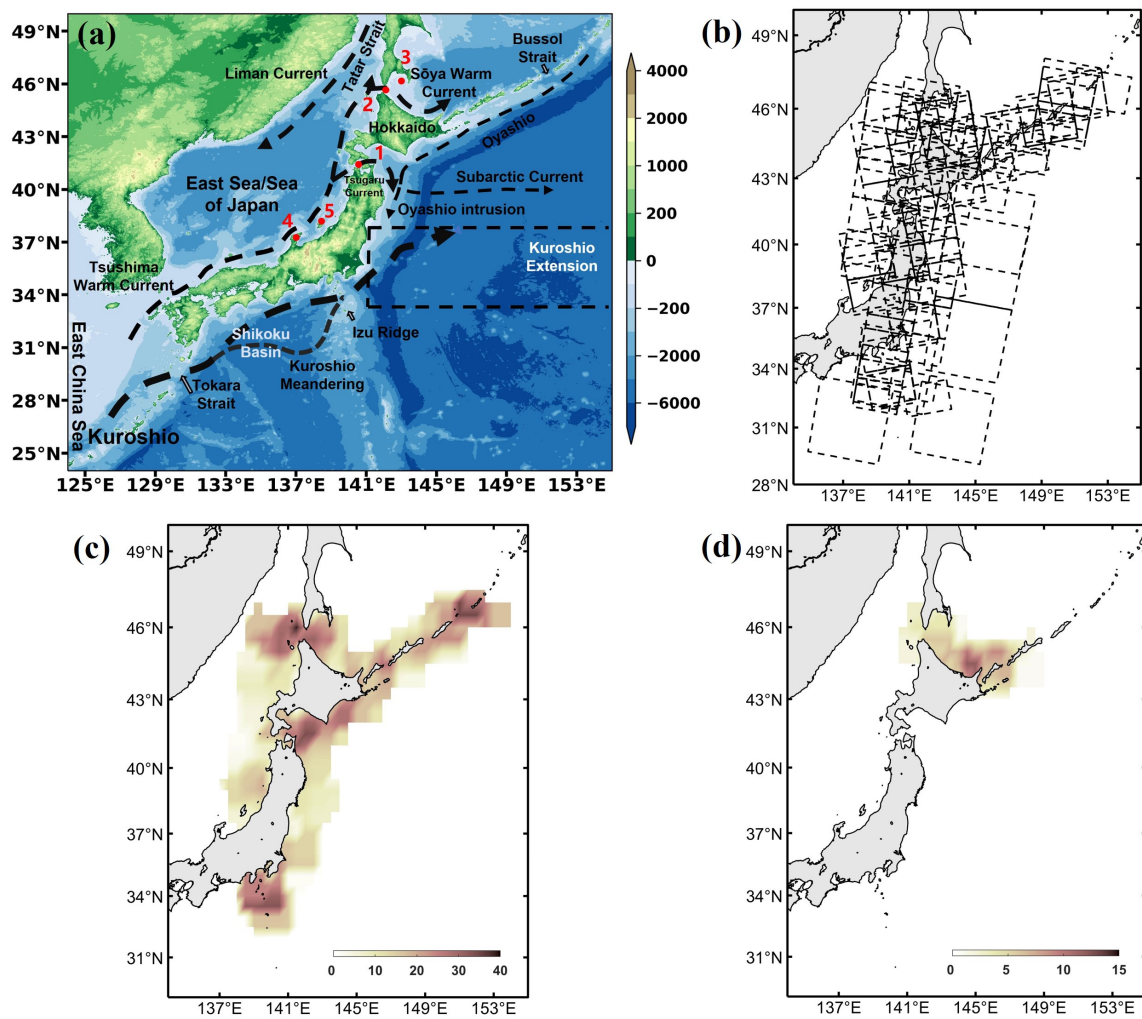


Figure 1. (a) The ocean currents around the Japanese coast along with the bottom topography (unit: m). (b) The positions of selected SAR images from 2015 to 2021; dashed rectangles are outlines of SAR images. Spatial coverage of SAR images for the coastal area (c) without ice and (d) with ice. The number of SAR images including eddies is shown by the color scale. The markers labeled with numbers 1–5 represent Tsugaru Strait, La Perouse Strait, Aniva Bay, Noto Peninsula, and Sado Island.

The coastal dynamic features controlled by coastlines, wind, and geostrophic currents have a strong effect on the generation and spatial distribution of submesoscale eddies [13,50]. The main characteristics of several typical background features are illustrated as shown below:

- Kuroshio meandering;

The Kuroshio meandering south of Japan has three typical paths, including a typical large meander and a non-large meander (NLM), which can further be divided into a nearshore and offshore NLM (nNLM and oNLM, respectively) [51]. Previous studies have considered that the wind forcing plays an important role in controlling the upstream volume transport, leading to a change in the Kuroshio path [10,52]. The internal oceanic processes (i.e., baroclinic instability and eddy–flow interaction) have been proven to be essential for the large meanders [53]. In addition, the interaction between the coastal turns/islands and the Kuroshio current provides favorable conditions to generate submesoscale eddies.

- Kuroshio–Oyashio Extension region;

The Kuroshio–Oyashio Extension region encompasses the Kuroshio Extension, the Oyashio, and its extension, which contain various frontal processes and mesoscale and sub-

mesoscale processes [54]. The Kuroshio flows eastward off Cape Inubozaki and contributes to the formation of submesoscale structures. The submesoscale eddies in this area depend almost completely on the conditions of the background currents and the topography, due to the strong western boundary currents.

- The Oyashio Current near the Tohoku Region;

The Oyashio Current, fed by cold and nutrient-rich upwelling water, flows southward from the subarctic North Pacific Ocean [55]. The current carries a large amount of material along the coast to the south. The interaction between the complicated capes and strong alongshore currents leads to the generation of submesoscale eddies.

- The Tsugaru Strait;

The Tsugaru Warm Current flows eastward in the Tsugaru Strait and turns south at Cape Shiriya. The Tairadate Strait connects Mutsu Bay to the Tsugaru Strait. This jet-like induced instability converts potential and kinetic energy from the mean fields to the eddy fields [56], which further contributes to the generation of submesoscale processes.

- The Tsushima Warm Current;

The coastal branch of the Tsushima Warm Current originates from the eastern side of the Tsushima Strait and flows along the Japanese coast, including Noto Peninsula and Sado Island. These topographic obstacles to coastal currents are a favorable factor in the development of submesoscale processes.

- The Kuril Islands (Russia);

Submesoscale eddies near the Kuril Islands have been investigated previously, revealing that they are caused by the interactions of coastal boundaries and the stretching of the current fields (e.g., the Sōya Warm Current and the Oyashio Current) [22]. This environmental condition contributes to the local generation of submesoscale eddies.

- The northern coast of Hokkaido;

The Sōya Warm Current flows southeastwardly along the coastal shallow region and its path becomes obscure behind Cape Shiretoko. Some mesoscale eddies form off Cape Shiretoko when the alongshore inflow of low-density waters intrudes into the deep basin [57]. The coast of Aniva Bay has Cape Krilion in the Soya Strait and Cape Aniva, which together facilitate the generation of submesoscale processes.

Submesoscale flows have been investigated in polar marginal ice zones [58,59] and ice-free ocean regions [36]. Serving as a kind of tracer, ice makes eddies and filaments prominently visible in SAR images because of the modulation of small-scale surface roughness impacted by wave–current interactions, the accumulation of drifting ice floes, and the wind variation across oceanic fronts. The northern coast of Hokkaido has ice floes in winter, which provide a good environment for detecting submesoscale “ice” eddy signatures in SAR imagery.

- The western coast of Hokkaido;

Four islands, including Rebun Island, Rishiri Island, Teuri Island, and Yagishiri Island, are located along the western coast of Hokkaido and contribute to the generation of submesoscale eddies via the process of topographic wake formation [11,60].

2.2. Sentinel-1 SAR Imagery

The Sentinel-1 SAR imagery can provide data with a 250 km swath at 5 m × 20 m spatial resolution in the Interferometric Wide (IW) swath mode, and the only/mostly IW mode data are available over the study site due to satellite flight trajectories. This mode is made up of three sub-swaths (IW1, IW2 and IW3) consisting of a series of bursts and it supports various dual polarization configurations (HH + HV and VV + VH) [61,62]. These advanced SAR imaging technologies have the ability to capture submesoscale oceanic processes, helping us to understand their generation in space. Oceanic submesoscale eddies

have been successfully detected from SAR images, taking advantage of the all-weather capability, at any time, day or night, with high sensitivity to small-scale variabilities of sea surface conditions [15,25,63]. In this study, high-resolution images were obtained from the Sentinel-1A and Sentinel-1B satellites at C-band with IW swath mode, from 2015 to 2021, downloaded from the Alaska Satellite Facility (<https://asf.alaska.edu>) (Figure 1b). The Level-1 Ground Range Detected products were post-processed to obtain the normalized radar cross sections (NRCSs) following previous work [64]. The SAR images were then further processed to enhance the grayscale contrast (using the contrast-limited adaptive histogram equalization method) and thus better identify eddies [65,66].

The seasonal distributions of all the images with distinct eddy signatures during the years 2015–2021 are summarized in Table 1. In total, 319 filtered Sentinel-1 images with distinct eddy signatures were analyzed to detect submesoscale eddies near the coastal regions of eastern Japan. Notably, the seasonal distribution of the number of SAR images was inhomogeneous. The images were mainly acquired in spring (March–April–May), summer (June–July–August) and autumn (September–October–November) (Table 1). Figure 1d shows that the SAR images within the ice zone mainly covered the La Perouse Strait, Aniva Bay, and the northern coastal area of Hokkaido in winter (December–January–February), while, outside the ice zone, there was good coverage of SAR images over the central and northern coastal areas (Figure 1c).

Table 1. Seasonal numbers of SAR images obtained from the Sentinel-1 satellite.

Year	Spring	Summer	Autumn	Winter	Total
2015	14	14	5	2	35
2016	5	7	2	0	14
2017	7	7	10	4	28
2018	9	10	16	3	38
2019	8	16	17	1	42
2020	17	26	27	7	77
2021	17	29	35	4	85
Total	77	109	112	21	319

2.3. Methods of the Eddy Feature Extraction

Although deep learning methods have been applied in submesoscale eddy detection from satellite images [15,16,24], there are not enough Sentinel-1 SAR images containing submesoscale eddies to provide training sets. As a result, in the previous, similar studies, eddy factors have tended to be (successfully) detected based on visual identification of surface signatures [32,36,50,59,67]. These surface signatures include the eddy center, four positions of the outer rectangular edges, the occurrence time, the rotation type, and the observed type of particular surface SAR signatures.

The center and outer rectangular edge of an eddy are derived manually as shown in Figure 2. The mean radius R_m ($R_m = (D1 + D2 + D3 + D4)/4$) is taken as the mean distance from the center to each side. Although this artificial perception method contains biases, our results obtained in this way have nonetheless captured the submesoscale eddies in SAR images and have also led to a comprehensive estimate of the number of submesoscale eddies along the Japanese coast.

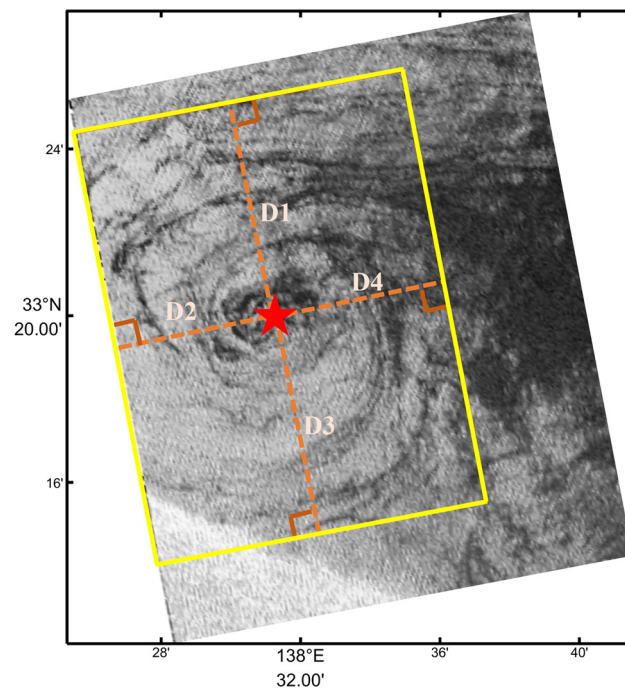


Figure 2. The schematic diagram of the eddy feature extraction procedure, using the SAR image on 8 November 2016 at 08:40 UTC as an example. The red star and rectangle are the center and shape of an eddy. The mean value of the distances from the center to each side (D1, D2, D3 and D4) is the mean radius of the eddy.

2.4. Other Supplementary Datasets

The monthly wind velocity at 10 m was taken from the NCEP Climate Forecast System reanalysis, version 2 (CFSv2; <http://cfs.ncep.noaa.gov>), which has a grid spacing of $0.205^\circ \times 0.204^\circ$ from 2015 to 2021. Three-hourly surface currents were obtained from the Hybrid Coordinate Ocean Model (HYCOM of Global Ocean Forecasting System 3.1 output on the grids of GLBv0.08, GLBu0.08 and GLBy0.08; <https://www.hycom.org>) with a spatial resolution of $1/12^\circ$. The daily data of chlorophyll concentration and sea surface temperature (SST) from MODIS-Aqua measurements were taken from the ocean color website Level-3 (4 km) data (<https://oceancolor.gsfc.nasa.gov>).

3. Results

3.1. Typical Signatures of Submesoscale Eddies near the Coastal Regions of Eastern Japan

Submesoscale eddies near the coastal regions of eastern Japan are classified into five typical signatures in SAR images: “black” eddy, “white” eddy, “ice” eddy, mushroom-like eddy pair, and a vortex street (Figure 3). “Black” eddies often appear in SAR imagery at low to moderate wind speeds, because the reduction of the backscatter cross-section due to natural films on the sea surface makes eddies look dark in SAR imagery (Figure 3a) [15,32]. At higher wind speeds, eddies with bright, curved lines are referred to as “white” eddies due to their higher backscatter cross-sections in SAR imagery, under the influence of wave–current interactions (Figure 3b) [15,32]. “Ice” eddies are visible in SAR imagery, due to the modulation of surface roughness in regions of accumulated drifting sea ice floes (Figure 3c), which is often seen in cyclonic eddies and filaments [36]. Here, another special type of submesoscale eddies is also a mushroom-like eddy pair as shown in Figure 3d. The cyclonic part of eddy signatures is more visible than the anticyclonic part, because cyclones generate surface convergence of ice and lead to greater sea ice thickness and concentration, while anticyclones reduce the sea ice concentration [59]. The last special type is a vortex street, as shown in Figure 3e. Previous work found that cyclones and anticyclones behave symmetrically in the small Ro/Bu regions [68]. Here, $Ro = U/fD$ is the Rossby number

and $Bu = (R_d/D)^2$ is the Burger number, where U is the velocity, D is the horizontal scale of the obstacle, f is the Coriolis parameter, and R_d is the baroclinic deformation radius.

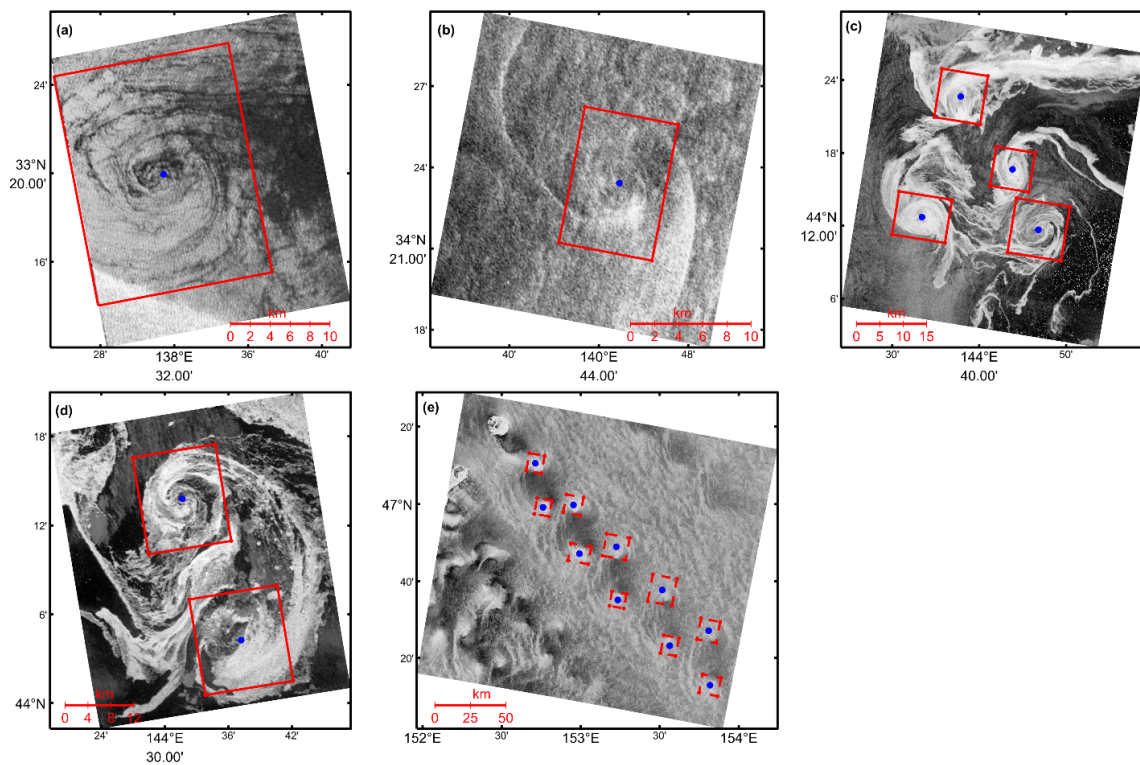


Figure 3. The typical signatures of submesoscale eddies near the coastal regions of eastern Japan, including (a) a “black” eddy sampled on 8 November 2016 at 08:40 UTC, (b) a “white” eddy sampled on 1 January 2017 at 20:43 UTC, (c) “ice” eddies inside the mesoscale cyclonic eddy sampled on 23 March 2018 at 20:24 UTC, (d) a mushroom-like eddy sampled on 8 March 2021 at 08:19 UTC, and (e) a vortex street (only one group marked) sampled on 20 May 2020 at 19:59 UTC. The blue dots and red rectangles are the centers and shapes of submesoscale eddies.

3.2. Spatial Scale and Spatial–Temporal Distributions of Submesoscale Eddies

We identified 1499 eddies near the coastal regions of eastern Japan based on 319 filtered Sentinel-1 images acquired between 2015 and 2021, around 98% of which were submesoscale eddies, and the first baroclinic Rossby radius of deformation was around 20 km during this period. The brighter features associated with higher wind speeds pose challenges for the detection of “white” eddies in SAR images. Due to these imaging features in SAR imagery, “black” eddies were visible more frequently than the other types near the coastal regions of eastern Japan (Figure 4). “Black” eddies constituted around 72% of all eddies, while “white” and “ice” eddies composed around 12% and 4%, respectively. The radius of the “black” and “white” eddies was predominately 2–6 km. The numbers of the mushroom-like eddies and vortex streets were too small to be counted.

The centers and radii of all eddies are marked in Figure 5. The locations of all the eddies are homogeneous along the Japanese coast. As we can see, all eddies are associated with the main strong currents that flow along the Japanese coast (Figure 1a). The characteristics of current fields and topographic features lead to the generations of submesoscale eddies in these several subregions, which will be discussed in the next section.

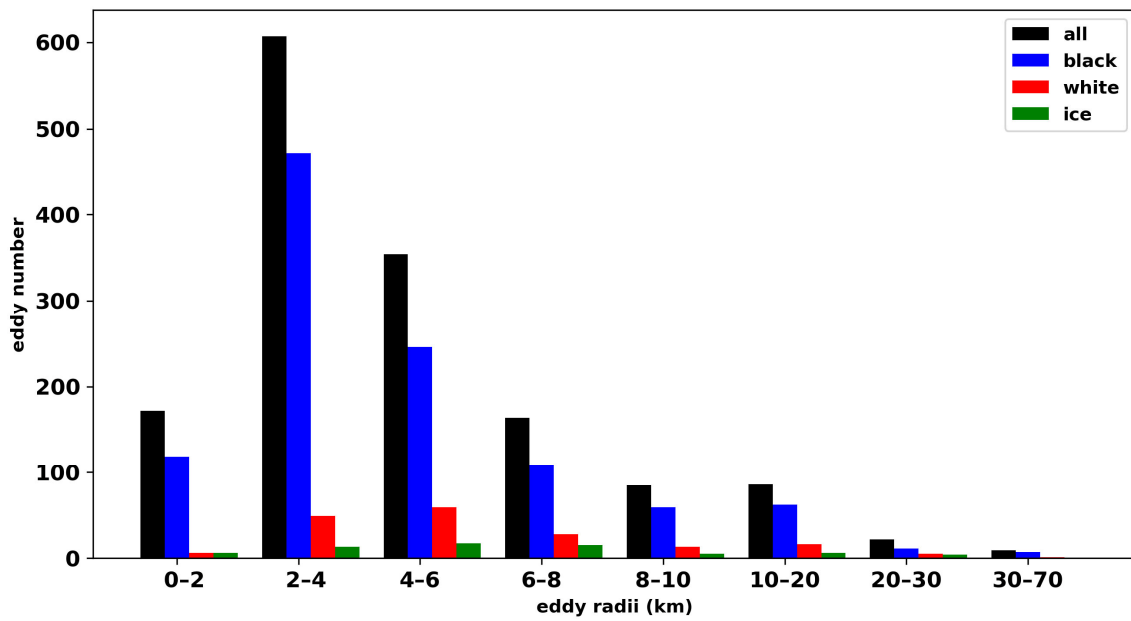


Figure 4. The histogram of the number of eddy radii (unit: km) identified from Sentinel-1 SAR imagery. The black, blue, red, and green bars indicate the number of all eddies, “black” eddies, “white” eddies, and “ice” eddies, respectively.

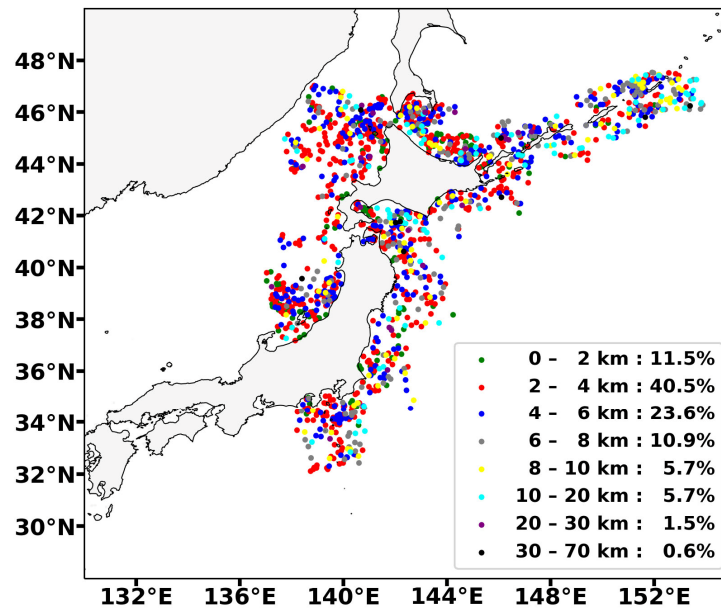


Figure 5. Locations of all eddies identified from Sentinel-1 SAR imagery during 2015–2021.

Figure 6a shows the annual number of eddies from 2015 to 2021, revealing that cyclonic eddies mainly dominate over anticyclonic eddies, with a ratio of around 78% cyclones to around 22% anticyclones. As the number of satellite images increases, shown in Table 1, the absolute quantity of detected eddies increases accordingly. The smallest number (around 8%) of submesoscale eddies is clearly in winter, while relatively larger numbers of submesoscale eddies occur in autumn, summer, and spring (Figure 6b). To reduce the effects of the number of Sentinel-1 images from month to month and year to year, the normalized eddy numbers are provided by normalizing the absolute eddy numbers to the corresponding number of images, for a given year (Figure 6c) and season (Figure 6d). A similar result is obtained for the dominant features of submesoscale cyclones and the very few submesoscale anticyclones. Nevertheless, the prominent result is that the

normalized numbers of cyclonic and anticyclonic eddies are almost the same every year, which illustrates that submesoscale eddies are commonly found near the coastal regions of eastern Japan and their numbers vary depending on the number of satellite images. Figure 6d indicates the ratio of the number of cyclonic/anticyclonic eddies to the total number of filtered satellite images.

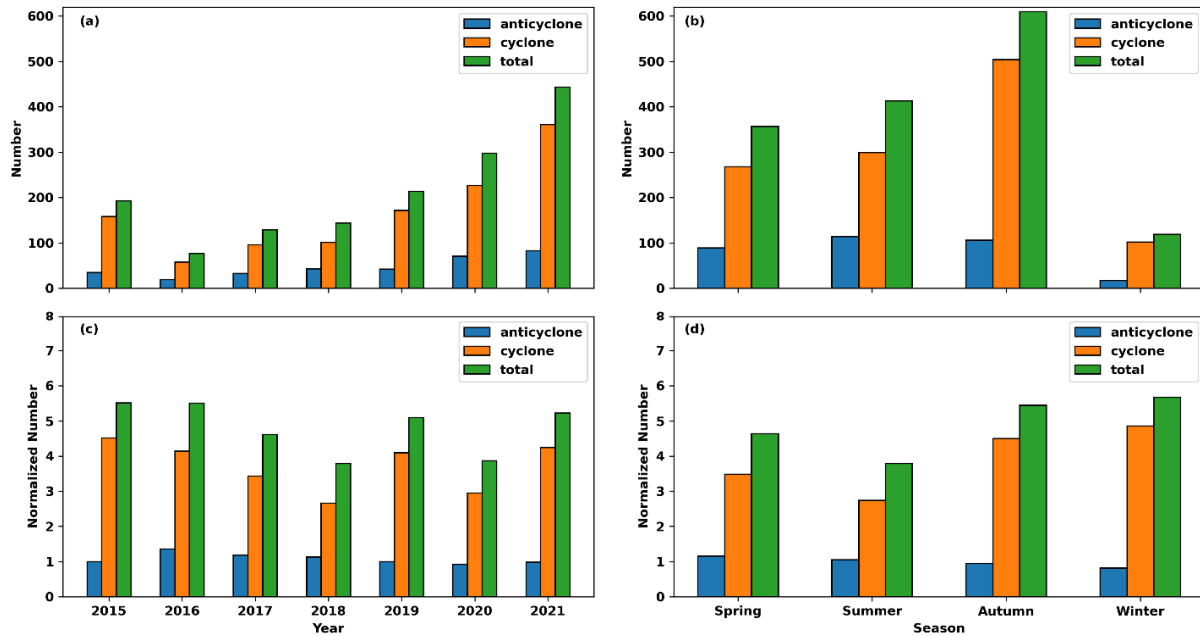


Figure 6. The (a,c) annual and (b,d) seasonal distributions of the (a,b) number and (c,d) normalized number of eddies detected from Sentinel-1 images during 2015–2021.

The ability to detect cyclonic/anticyclonic submesoscale eddies from every Sentinel-1 image containing eddy characteristics is almost the same each season, which demonstrates that submesoscale cyclonic eddies are found more frequently than anticyclonic eddies. This also shows no seasonality in the normalized numbers for detected cyclonic/anticyclonic eddies for each image (Figure 6d). Compared with Figure 6d, the absolute number of cyclonic/anticyclonic eddies (Figure 6b) is the most prominent feature resulting from the seasonal variation of the surface 10 m winds. Figure 7 shows the seasonally averaged 10 m surface winds near the coastal regions of eastern Japan from 2015 to 2021. Thus, the highest wind speed is in winter, at over 6 m/s in most regions, corresponding to the lowest absolute number of submesoscale eddies in winter. The brighter features in the SAR images, in winter, with relatively high wind speeds, make it difficult to detect eddies in such images. Strong winds in winter could disrupt surface natural slicks, enhancing noise in SAR images due to saturated backscattering, thereby hindering the identification of eddies [15]. In other seasons, lower wind speeds and fewer natural slicks result in weak backscattering, thereby enhancing the prominence of the spiral characteristics of eddies. This condition is beneficial to eddy detection [69].

In general, we found that submesoscale cyclones are typically more common than submesoscale anticyclonic eddies, which is similar to the findings of previous studies [25,36]. Cyclonic eddies often have a larger intensity with higher Ro , as compared to anticyclonic eddies which become unstable with high Ro ($Ro > 1$) owing to centrifugal instability [70]. In addition, intense submesoscale cyclonic eddies also have strong impacts on surface tracers, which increases their visibility and leads to their more frequent detection.

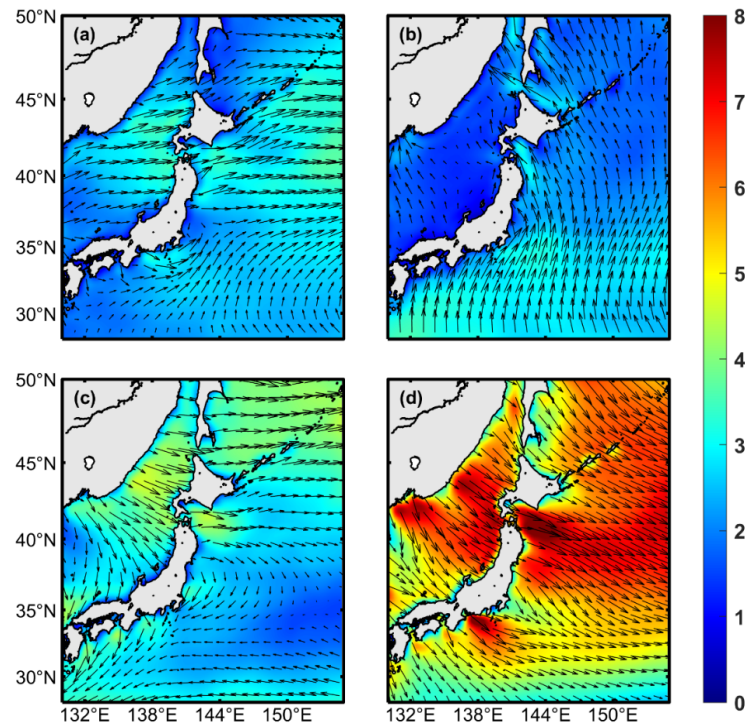


Figure 7. Seasonally averaged distributions of NCEP 10 m winds (shading: velocity, unit: m s^{-1}) from 2015 to 2021 for (a) spring, (b) summer, (c) autumn, and (d) winter.

4. Discussion: Generation Mechanisms

The main mechanisms for the generation of submesoscale eddies near the coastal regions of eastern Japan are summarized schematically in Figures 8 and 9. Submesoscale cyclonic eddies are often observed inside mesoscale cyclonic eddies (Figure 8a) and at the periphery of mesoscale anticyclonic eddies (blue eddies in Figure 8b). Inside cyclones, the same cyclonic shears and vorticity gradients lead to the formation of submesoscale cyclonic eddies (Figure 8(a1,a2)), especially in zones with ice floes (Figure 8(a3,a4)), primarily due to vertical buoyancy fluxes [71]. The features of spiral eddies are often seen in SAR images where strong cyclonic shears lead to streaks and shear instability generates convergence. It has been found that submesoscale cyclonic eddies trap sea ice, whereas anticyclonic eddies reduce its accumulation [72]. Similarly, submesoscale anticyclones can also be found inside mesoscale anticyclones (the red eddy in Figure 8b) probably owing to both vertical shear production and vertical buoyancy fluxes [71]. Cyclonic shear and a high vorticity gradient at the periphery of anticyclonic eddies (Figure 8(b1,b2)) often contribute to the generation of submesoscale cyclonic eddies (the blues eddies in Figure 8b). Along with the effect of topography, sometimes these mechanisms can reinforce each other. Submesoscale anticyclonic eddies are rarely detected at the edge of mesoscale cyclonic eddies, probably due to the weak vorticity gradients at the edges [73]. Indeed, submesoscale cyclones are detected more frequently at the periphery of mesoscale cyclones [50].

The third mechanism of mushroom-like structures is associated with the deceleration of a strong current (jet) forced by horizontal shear, or the collision between different water masses (Figure 8c) [74]. As shown in Figure 8(c1,c2), the alongshore jet detaches from the cape and collides with the drifting ice floes and meets the marginal ice zone flowing northeastward, which decelerates the jet and leads to horizontal shear, convergence, and dipole eddies. This kind of formation can also be found near river mouths [50].

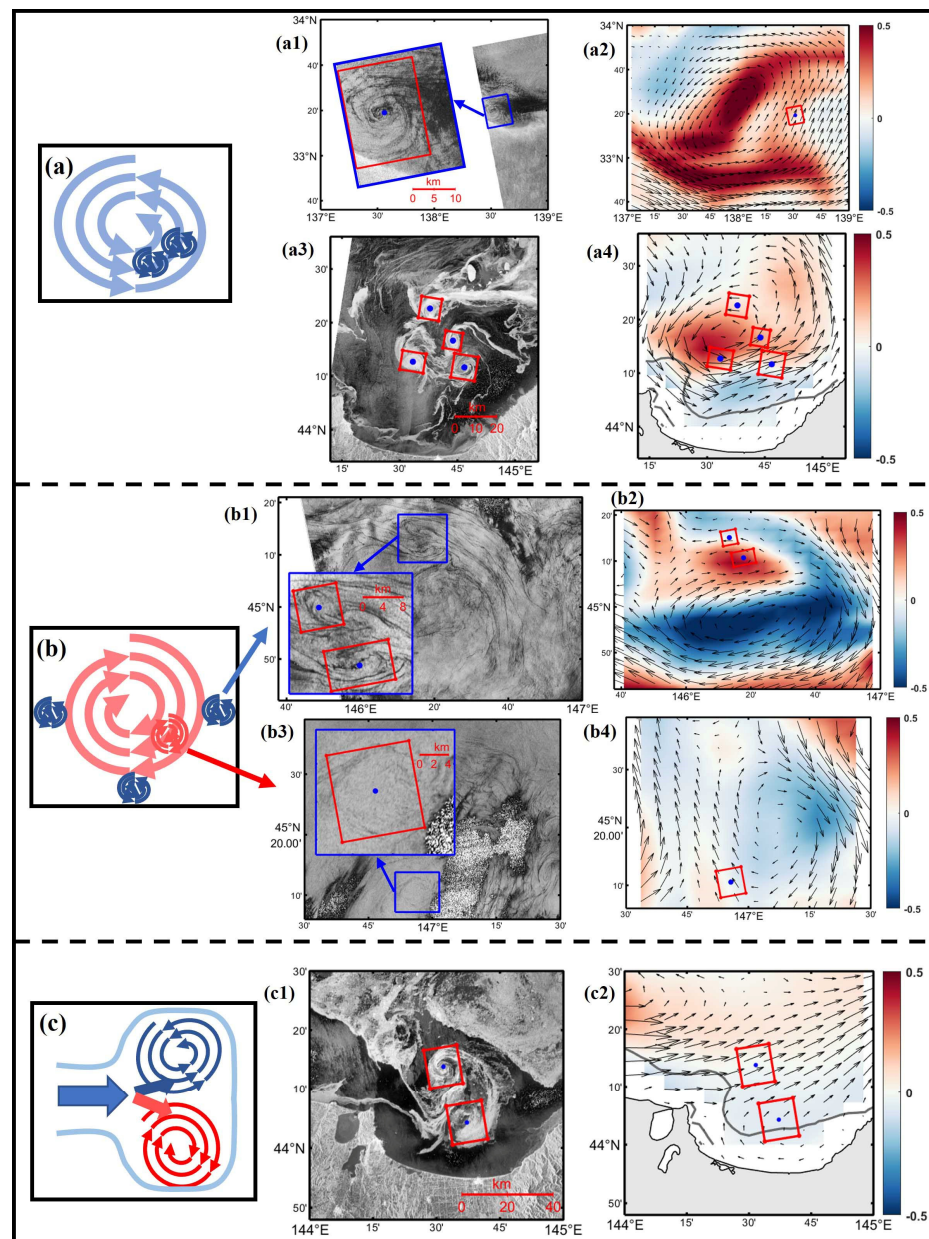


Figure 8. Schematic 1 of the main mechanisms of submesoscale eddies near the coastal regions of eastern Japan and corresponding cases: **(a)** submesoscale cyclonic eddies inside a mesoscale cyclone, with examples shown in **(a1)** for the cyclonic eddy on 8 November 2016 at 08:40 UTC and in **(a3)** for the cyclonic eddies with sea ice on 23 March 2018 at 20:24 UTC; **(b)** submesoscale cyclonic eddies at the periphery of a mesoscale anticyclone and anticyclonic eddies inside the eddy, with examples shown in **(b1)** for the cyclonic eddies at the periphery on 10 September 2018 at 08:02 UTC and in **(b3)** for the anticyclonic eddy inside the eddy on 23 October 2019 at 08:03 UTC; **(c)** a submesoscale mushroom-like eddy pair due to the deceleration of the jet, with an example shown in **(c1)** for the eddy pair on 8 March 2021 at 08:19 UTC. The corresponding HYCOM currents with their relative vorticity (unit: dimensionless) are depicted at the nearest time to the SAR imagery **(a2,a4,b2,b4,c2)**, overlaying 100 m isobaths (gray lines). The blue dots and red rectangles represent the centers and shapes of submesoscale eddies. The magnified images depict intricate eddy structures in detail (blue rectangles).

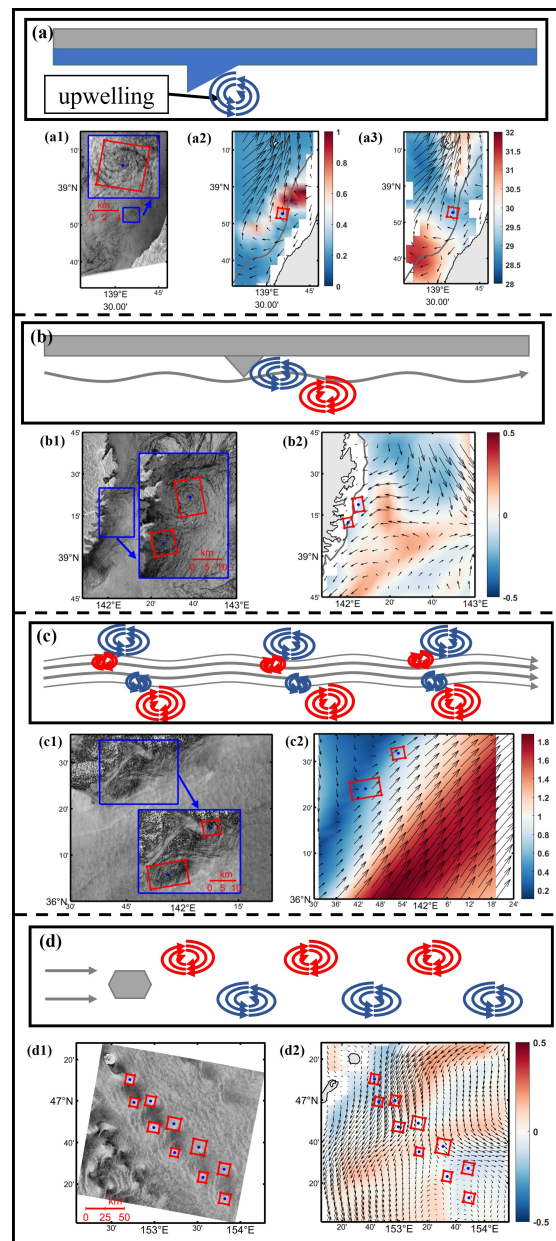


Figure 9. Schematic 2 of the main mechanisms of submesoscale eddies near the coastal regions of eastern Japan: (a) submesoscale eddies due to baroclinic instability in coastal upwelling regions, with an example shown in (a1) for the submesoscale eddies on 2 August 2021 at 08:42 UTC; (b) submesoscale eddies due to the separation of the alongshore current, with an example shown in (b1) for the submesoscale cyclonic eddies on 17 October 2015 at 08:26 UTC; (c) submesoscale eddies due to shear instability at the strong current, with an example shown in (c1) for the submesoscale eddies on 18 November 2020 at 08:33 UTC; (d) a submesoscale vortex street due to island wakes, with an example shown in (d1) for the submesoscale eddies on 20 May 2020 at 19:59 UTC. The HYCOM currents with their relative vorticity (unit: dimensionless) are depicted at the nearest time of SAR imagery (b2,d2), overlaying 100 m isobaths (gray lines). The HYCOM currents with (a2) chlorophyll concentration (unit: mg m^{-3}) and (a3) SST (unit: $^{\circ}\text{C}$) are depicted at the nearest time of SAR imagery, overlaying 100 m isobaths (gray lines). The HYCOM currents with their velocity (unit: m/s) are depicted at the nearest time to the SAR imagery (c2), overlaying 100 m isobaths (gray lines). The blue dots and red rectangles represent the centers and shapes of submesoscale eddies. The magnified images depict intricate eddy structures in detail (blue rectangles).

Submesoscale eddies can form due to upwelling-induced instability (Figure 9a) where the dense, cold upwelling flows over the lighter offshore water, thereby leading to re-stratification and the formation of submesoscale eddies. The high values of chlorophyll concentration (Figure 9(a2)) and the low values of SST (Figure 9(a3)) correspond to the upwelling region, where a submesoscale eddy is detected (Figure 9(a1)). According to previous studies [4,75,76], the mixed layer instability due to restratification in the mixed layer is conducive to the generation of submesoscale eddies.

The next mechanism is the most common (Figure 9b), involving flow separation near capes and turns. When the alongshore current or jet flows near a cape/turn, a low-pressure region is formed behind the cape/turn owing to the separation of the current and the centrifugal forces. Then, submesoscale eddies are generated, as the flow rotates near the cape/turn (Figure 9(b1,b2)). The interactions between the background flow fields and topographic features make submesoscale eddies form near the cape/turn [50].

Shear vorticity and orbital vorticity tend to appear in strong currents with meanders that have a strong velocity shear and vorticity gradient (Figure 9c). The vorticity adjustment due to the centrifugal force in the meander generates submesoscale eddies (Figure 9(c1,c2)) near the main axis of the strong currents [77]. This kind of submesoscale eddy is commonly found in the global ocean.

We found a specific example of the mechanism of a submesoscale Kármán vortex street in this study around Ketoy Island (Figure 9d). Like island wakes, vortex streets consist of two sets of staggered vortices with different directions of rotation (Figure 9(d1)) [78]. The interaction between the background flow fields (Figure 9(d2)) and the islands is the main reason for vortex streets. Under specified conditions, island wakes could develop into a Kármán vortex street [68,79].

In summary, we have described the characteristics of submesoscale eddies near the coastal regions of eastern Japan and discussed some of the probable underlying mechanisms. These phenomena and their generative development make it more challenging to further understand coastal submesoscale processes and dynamics. However, quantifying detailed generation mechanisms for each process mentioned is challenging, due to the extensive numerical simulations and validations required. Visual identification has been applied in the identification of surface eddy signatures. But this has human error. It is therefore important to develop and utilize deep learning techniques to automate the detection of eddy signatures in SAR satellite images. This is also the topic of further work.

Satellite optical data also plays a crucial role in capturing submesoscale eddies in the global ocean [56,80,81]. When combined with multi-sensor satellite imagery, this method offers a more comprehensive framework for capturing and analyzing the generation and evolution of eddies, thereby augmenting our comprehension of the characteristics of submesoscale eddies off the Japanese coast and even in the global ocean. Aside from HYCOM, there are few products with higher spatial and temporal resolutions that can provide long-term background flow fields for this region. While the spatial resolution of the HYCOM flow fields may be considered relatively low, it still provides valuable background field information. This information can provide a qualitative mechanism for the phenomenon by correlating the positions of eddies in the SAR images with those of the flow field, drawing upon prior research. While HYCOM can provide background information regarding the flow field, its resolution is too coarse to directly characterize the structure of the submesoscale flow fields. Additionally, although most of the eddies we have detected are located where the water depth exceeds 100 m, the accuracy of HYCOM outputs near the coasts (over depth < 100 m) may be questionable due to the assimilation of “incorrect altimetry measurements”. Therefore, high-resolution coastal numerical simulations are needed for diagnostic analysis in further studies.

5. Conclusions

This study collected 319 filtered Sentinel-1 images near the coastal regions of eastern Japan during 2015–2021 to identify submesoscale eddies and qualitatively analyze their

spatiotemporal distributions. In total, 1499 eddies were detected from SAR images, of which around 98% were submesoscale eddies, with a ratio of around 78% cyclones to around 22% anticyclones. The number of submesoscale eddies was relatively small in winter owing to the stronger, 10 m wind speeds compared to other seasons. The normalized numbers of cyclonic and anticyclonic eddies in each image are almost the same every year, with cyclonic eddies being more frequently detected in SAR images than anticyclonic eddies.

The probable mechanisms of the generation of submesoscale eddies were categorized as: (1) cyclonic/anticyclonic shear inside mesoscale cyclones/anticyclones, (2) cyclonic shear at the periphery of mesoscale anticyclonic eddies, (3) deceleration of a strong current (jet) forced by horizontal shear or the collision between different water masses, (4) separation of the current and the centrifugal forces behind capes/turns, (5) velocity shear and the vorticity gradient near currents with meanders, and (6) the interaction between background flow fields and islands.

Sentinel-1 images successfully capture the submesoscale features near most of the Japanese coast and thus help us to better understand submesoscale processes in this region. The analysis performed in this study can provide characteristics of submesoscale eddy activity along the Japanese coast. This serves as a foundation for the subsequent construction and validation of submesoscale numerical simulations in this region. Additionally, this study can offer supplementary data support when optical imagery is insufficient for observations in this area.

Author Contributions: Conceptualization, G.L. (Gang Li) and Y.H.; methodology, G.L. (Gang Li); validation, G.L. (Gang Li), G.L. (Guoqiang Liu) and Y.H.; formal analysis, Y.H. and V.K.; investigation, G.L. (Gang Li), J.W. and X.L.; writing—original draft preparation, G.L. (Gang Li); writing—review and editing, V.K. and W.P.; supervision, Y.H. All authors have read and agreed to the published version of the manuscript.

Funding: This research was funded by the National Natural Science Foundation of China under grants 42027805, and the Postgraduate Research & Practice Innovation Program of Jiangsu Province under grant KYCX21_0959.

Institutional Review Board Statement: Not applicable.

Informed Consent Statement: Not applicable.

Data Availability Statement: Sentinel-1 images were downloaded from the Alaska Satellite Facility (<https://search.asf.alaska.edu/#/>, accessed on 30 April 2024). The currents of HYCOM are available online (<https://tds.hycom.org/thredds/catalog.html>, accessed on 30 April 2024). The monthly wind velocity data at 10 m were obtained from the NECP Climate Forecast System reanalysis (<https://rda.ucar.edu/datasets/ds094.2/>, accessed on 30 April 2024).

Acknowledgments: We acknowledge the High Performance Computing Center of Nanjing University of Information Science & Technology for their support of this work. Thanks to Xiaoheng Mou for data pre-processing. Thanks to Huimin Li for proofreading the content of this article.

Conflicts of Interest: The authors declare no conflicts of interest.

References

1. Sun, W.; Liu, Y.; Chen, G.; Tan, W.; Lin, X.; Guan, Y.; Dong, C. Three-dimensional properties of mesoscale cyclonic warm-core and anticyclonic cold-core eddies in the South China Sea. *Acta Oceanol. Sin.* **2021**, *40*, 17–29. [\[CrossRef\]](#)
2. Sun, W.; Yang, J.; Tan, W.; Liu, Y.; Zhao, B.; He, Y.; Dong, C. Eddy diffusivity and coherent mesoscale eddy analysis in the Southern Ocean. *Acta Oceanol. Sin.* **2021**, *40*, 1–16. [\[CrossRef\]](#)
3. Ueno, H.; Bracco, A.; Barth, J.A.; Budyansky, M.V.; Hasegawa, D.; Itoh, S.; Kim, S.Y.; Ladd, C.; Lin, X.; Park, Y.-G.; et al. Review of oceanic mesoscale processes in the North Pacific: Physical and biogeochemical impacts. *Prog. Oceanogr.* **2023**, *212*, 102955. [\[CrossRef\]](#)
4. Thomas, L.N.; Tandon, A.; Mahadevan, A. Submesoscale processes and dynamics. In *Ocean Modeling in an Eddy Regime*; Geophysical Monograph Series; American Geophysical Union: Washington, DC, USA, 2008; pp. 17–38.
5. Zhang, Z.; Zhang, X.; Qiu, B.; Zhao, W.; Zhou, C.; Huang, X.; Tian, J. Submesoscale Currents in the Subtropical Upper Ocean Observed by Long-Term High-Resolution Mooring Arrays. *J. Phys. Oceanogr.* **2021**, *51*, 187–206. [\[CrossRef\]](#)

6. Brett, G.J.; Whitt, D.B.; Long, M.C.; Bryan, F.O.; Feloy, K.; Richards, K.J. Submesoscale Effects on Changes to Export Production Under Global Warming. *Glob. Biogeochem. Cycles* **2023**, *37*, e2022GB007619. [[CrossRef](#)]
7. Taylor, J.R.; Thompson, A.F. Submesoscale Dynamics in the Upper Ocean. *Annu. Rev. Fluid Mech.* **2023**, *55*, 103–127. [[CrossRef](#)]
8. Zhang, Z.; Liu, Y.; Qiu, B.; Luo, Y.; Cai, W.; Yuan, Q.; Liu, Y.; Zhang, H.; Liu, H.; Miao, M.; et al. Submesoscale inverse energy cascade enhances Southern Ocean eddy heat transport. *Nat. Commun.* **2023**, *14*, 1335. [[CrossRef](#)] [[PubMed](#)]
9. Takahashi, D.; Endo, H.; Minegishi, Y.; Gomi, Y.; Kaneko, K. Wind- and density-driven circulation in a bay on the Sanriku ria coast, Japan: Study of Shizugawa Bay facing the Pacific Ocean. *J. Oceanogr.* **2018**, *74*, 81–100. [[CrossRef](#)]
10. Tsujino, H.; Nishikawa, S.; Sakamoto, K.; Usui, N.; Nakano, H.; Yamanaka, G. Effects of large-scale wind on the Kuroshio path south of Japan in a 60-year historical OGCM simulation. *Clim. Dyn.* **2013**, *41*, 2287–2318. [[CrossRef](#)]
11. Masunaga, E.; Uchiyama, Y.; Zhang, X.; Kimura, W.; Kosako, T. Modulation of submesoscale motions due to tides and a shallow ridge along the Kuroshio. *Deep Sea Res. Part I Oceanogr. Res. Pap.* **2022**, *186*, 103828. [[CrossRef](#)]
12. Yang, Y.; San Liang, X. On the Seasonal Eddy Variability in the Kuroshio Extension. *J. Phys. Oceanogr.* **2018**, *48*, 1675–1689. [[CrossRef](#)]
13. Bashmachnikov, I.L.; Kozlov, I.E.; Petrenko, L.A.; Glok, N.I.; Wekerle, C. Eddies in the North Greenland Sea and Fram Strait From Satellite Altimetry, SAR and High-Resolution Model Data. *J. Geophys. Res. Ocean.* **2020**, *125*, e2019JC015832. [[CrossRef](#)]
14. Hamze-Ziabari, S.M.; Foroughan, M.; Lemmin, U.; Barry, D.A. Monitoring Mesoscale to Submesoscale Processes in Large Lakes with Sentinel-1 SAR Imagery: The Case of Lake Geneva. *Remote Sens.* **2022**, *14*, 4967. [[CrossRef](#)]
15. Ji, Y.; Xu, G.; Dong, C.; Yang, J.; Xia, C. Submesoscale eddies in the East China Sea detected from SAR images. *Acta Oceanol. Sin.* **2021**, *40*, 18–26. [[CrossRef](#)]
16. Xia, L.; Chen, G.; Chen, X.; Ge, L.; Huang, B. Submesoscale oceanic eddy detection in SAR images using context and edge association network. *Front. Mar. Sci.* **2022**, *9*, 1023624. [[CrossRef](#)]
17. Lin, H.; Liu, Z.; Hu, J.; Menemenlis, D.; Huang, Y. Characterizing meso- to submesoscale features in the South China Sea. *Prog. Oceanogr.* **2020**, *188*, 102420. [[CrossRef](#)]
18. Mukherjee, S.; Wilson, D.; Jobsis, P.; Habtes, S. Numerical modeling of internal tides and submesoscale turbulence in the US Caribbean regional ocean. *Sci. Rep.* **2023**, *13*, 1091. [[CrossRef](#)]
19. Itoh, S.; Tsutsumi, E.; Masunaga, E.; Sakamoto, T.T.; Ishikawa, K.; Yanagimoto, D.; Hoshihara, Y.; Kaneko, H.; Hasegawa, D.; Tanaka, K.; et al. Seasonal Cycle of the Confluence of the Tsugaru Warm, Oyashio, and Kuroshio Currents East of Japan. *J. Geophys. Res. Ocean.* **2022**, *127*, e2022JC018556. [[CrossRef](#)]
20. Li, C.; Zhang, Z.; Zhao, W.; Tian, J. A statistical study on the subthermocline submesoscale eddies in the northwestern Pacific Ocean based on Argo data. *J. Geophys. Res. Ocean.* **2017**, *122*, 3586–3598. [[CrossRef](#)]
21. Nagano, A.; Hasegawa, T.; Ariyoshi, K.; Iinuma, T.; Fukuda, T.; Fujii, N.; Tomita, F.; Hino, R. USV-Observed Turbulent Heat Flux Induced by Late Spring Cold Dry Air Incursion over Sub-Mesoscale Warm Regions off Sanriku, Japan. *Sensors* **2022**, *22*, 9695. [[CrossRef](#)]
22. Nakamura, T.; Matthews, J.P.; Awaji, T.; Mitsudera, H. Submesoscale eddies near the Kuril Straits: Asymmetric generation of clockwise and counterclockwise eddies by barotropic tidal flow. *J. Geophys. Res. Ocean.* **2012**, *117*, C12014. [[CrossRef](#)]
23. Takikawa, T.; Morimoto, A.; Onitsuka, G. Subsurface nutrient maximum and submesoscale structures in the southwestern Japan Sea. *J. Oceanogr.* **2016**, *72*, 529–540. [[CrossRef](#)]
24. Wang, Y.; Yang, J.; Wu, K.; Hou, M.; Chen, G. A Submesoscale Eddy Identification Dataset Derived from GOCI I Chlorophyll-a Data based on Deep Learning. *Earth Syst. Sci. Data Discuss.* **2023**, *2023*, 1–23. [[CrossRef](#)]
25. Atadzhanova, O.; Zimin, A.; Romanenkov, D.; Kozlov, I. Satellite radar observations of small eddies in the White, Barents and Kara Seas. *Phys. Oceanogr.* **2017**, *2*, 75–83. [[CrossRef](#)]
26. Hamze-Ziabari, S.M.; Razmi, A.M.; Lemmin, U.; Barry, D.A. Detecting Submesoscale Cold Filaments in a Basin-Scale Gyre in Large, Deep Lake Geneva (Switzerland/France). *Geophys. Res. Lett.* **2022**, *49*, e2021GL096185. [[CrossRef](#)]
27. Johannessen, J.A.; Kudryavtsev, V.; Akimov, D.; Eldevik, T.; Winther, N.; Chapron, B. On radar imaging of current features: 2. Mesoscale eddy and current front detection. *J. Geophys. Res. Ocean.* **2005**, *110*, C07017. [[CrossRef](#)]
28. Kudryavtsev, V.; Akimov, D.; Johannessen, J.; Chapron, B. On radar imaging of current features: 1. Model and comparison with observations. *J. Geophys. Res. Ocean.* **2005**, *110*, C07016. [[CrossRef](#)]
29. Kudryavtsev, V.; Myasoedov, A.; Chapron, B.; Johannessen, J.A.; Collard, F. Imaging mesoscale upper ocean dynamics using synthetic aperture radar and optical data. *J. Geophys. Res. Ocean.* **2012**, *117*, C04029. [[CrossRef](#)]
30. Kostianoy, A.G.; Ginzburg, A.I.; Lavrova, O.Y.; Mityagina, M.I. Satellite Remote Sensing of Submesoscale Eddies in the Russian Seas. In *The Ocean in Motion: Circulation, Waves, Polar Oceanography*; Velarde, M.G., Tarakanov, R.Y., Marchenko, A.V., Eds.; Springer International Publishing: Cham, Switzerland, 2018; pp. 397–413.
31. Kozlov, I.E.; Plotnikov, E.V.; Manucharyan, G.E. Brief Communication: Mesoscale and submesoscale dynamics in the marginal ice zone from sequential synthetic aperture radar observations. *Cryosphere* **2020**, *14*, 2941–2947. [[CrossRef](#)]
32. Karimova, S. Spiral eddies in the Baltic, Black and Caspian seas as seen by satellite radar data. *Adv. Space Res.* **2012**, *50*, 1107–1124. [[CrossRef](#)]
33. DiGiacomo, P.M.; Holt, B. Satellite observations of small coastal ocean eddies in the Southern California Bight. *J. Geophys. Res. Ocean.* **2001**, *106*, 22521–22543. [[CrossRef](#)]

34. Johannessen, J.A.; Shuchman, R.A.; Digranes, G.; Lyzenga, D.R.; Wackerman, C.; Johannessen, O.M.; Vachon, P.W. Coastal ocean fronts and eddies imaged with ERS 1 synthetic aperture radar. *J. Geophys. Res. Ocean.* **1996**, *101*, 6651–6667. [[CrossRef](#)]
35. Shu, S.; Yang, J.; Yang, C.; Hu, H.; Jing, W.; Hu, Y.; Li, Y. Performance Analysis of Ocean Eddy Detection and Identification by L-Band Compact Polarimetric Synthetic Aperture Radar. *Remote Sens.* **2021**, *13*, 4905. [[CrossRef](#)]
36. Kozlov, I.E.; Artamonova, A.V.; Manucharyan, G.E.; Kubryakov, A.A. Eddies in the Western Arctic Ocean From Spaceborne SAR Observations Over Open Ocean and Marginal Ice Zones. *J. Geophys. Res. Ocean.* **2019**, *124*, 6601–6616. [[CrossRef](#)]
37. Karimova, S.; Gade, M. Improved statistics of sub-mesoscale eddies in the Baltic Sea retrieved from SAR imagery. *Int. J. Remote Sens.* **2016**, *37*, 2394–2414. [[CrossRef](#)]
38. Liu, Z.; Gan, J.; Hu, J.; Wu, H.; Cai, Z.; Deng, Y. Progress of Studies on Circulation Dynamics in the East China Sea: The Kuroshio Exchanges With the Shelf Currents. *Front. Mar. Sci.* **2021**, *8*, 620910. [[CrossRef](#)]
39. Nakamura, H. Changing Kuroshio and Its Affected Shelf Sea: A Physical View. In *Changing Asia-Pacific Marginal Seas*; Chen, C.-T.A., Guo, X., Eds.; Springer: Singapore, 2020; pp. 265–305.
40. Qu, T.; Tozuka, T.; Kida, S.; Guo, X.; Miyazawa, Y.; Liu, Q. Western Pacific and Marginal Sea Processes. In *Indo-Pacific Climate Variability and Predictability*; World Scientific Series on Asia-Pacific Weather and Climate; World Scientific: Singapore, 2016; Volume 7, pp. 151–186.
41. Steele, J.H.; Thorpe, S.A.; Turekian, K.K. *Ocean Currents*; Academic Press: Cambridge, MA, USA, 2010.
42. Sugimoto, S.; Qiu, B.; Schneider, N. Local Atmospheric Response to the Kuroshio Large Meander Path in Summer and Its Remote Influence on the Climate of Japan. *J. Clim.* **2021**, *34*, 3571–3589. [[CrossRef](#)]
43. Matsuta, T.; Masumoto, Y. Modified View of Energy Budget Diagram and Its Application to the Kuroshio Extension Region. *J. Phys. Oceanogr.* **2021**, *51*, 1163–1175. [[CrossRef](#)]
44. Isobe, A.; Ando, M.; Watanabe, T.; Senjyu, T.; Sugihara, S.; Manda, A. Freshwater and temperature transports through the Tsushima-Korea Straits. *J. Geophys. Res. Ocean.* **2002**, *107*, 2-1–2-20. [[CrossRef](#)]
45. Ito, M.; Morimoto, A.; Watanabe, T.; Katoh, O.; Takikawa, T. Tsushima Warm Current paths in the southwestern part of the Japan Sea. *Prog. Oceanogr.* **2014**, *121*, 83–93. [[CrossRef](#)]
46. Mitsudera, H.; Uchimoto, K.; Nakamura, T. Rotating Stratified Barotropic Flow over Topography: Mechanisms of the Cold Belt Formation off the Soya Warm Current along the Northeastern Coast of Hokkaido. *J. Phys. Oceanogr.* **2011**, *41*, 2120–2136. [[CrossRef](#)]
47. Choi, J.; Park, Y.G.; Kim, W.; Kim, Y.H. Characterization of Submesoscale Turbulence in the East/Japan Sea Using Geostationary Ocean Color Satellite Images. *Geophys. Res. Lett.* **2019**, *46*, 8214–8223. [[CrossRef](#)]
48. Fayman, P.; Ostrovskii, A.; Lobanov, V.; Park, J.-H.; Park, Y.-G.; Sergeev, A. Submesoscale eddies in Peter the Great Bay of the Japan/East Sea in winter. *Ocean. Dyn.* **2019**, *69*, 443–462. [[CrossRef](#)]
49. Yoon, J.-H.; Kim, Y.-J. Review on the seasonal variation of the surface circulation in the Japan/East Sea. *J. Mar. Syst.* **2009**, *78*, 226–236. [[CrossRef](#)]
50. Aleskerova, A.; Kubryakov, A.; Stanichny, S.; Medvedeva, A.; Plotnikov, E.; Mizyuk, A.; Verzhvetskaia, L. Characteristics of topographic submesoscale eddies off the Crimea coast from high-resolution satellite optical measurements. *Ocean. Dyn.* **2021**, *71*, 655–677. [[CrossRef](#)]
51. Kawabe, M. Variations of Current Path, Velocity, and Volume Transport of the Kuroshio in Relation with the Large Meander. *J. Phys. Oceanogr.* **1995**, *25*, 3103–3117. [[CrossRef](#)]
52. Yang, Y.; San Liang, X. New Perspectives on the Generation and Maintenance of the Kuroshio Large Meander. *J. Phys. Oceanogr.* **2019**, *49*, 2095–2113. [[CrossRef](#)]
53. Liu, X.; Mu, M.; Wang, Q. The Nonlinear Optimal Triggering Perturbation of the Kuroshio Large Meander and Its Evolution in a Regional Ocean Model. *J. Phys. Oceanogr.* **2018**, *48*, 1771–1786. [[CrossRef](#)]
54. Itoh, S.; Yasuda, I. Characteristics of Mesoscale Eddies in the Kuroshio–Oyashio Extension Region Detected from the Distribution of the Sea Surface Height Anomaly. *J. Phys. Oceanogr.* **2010**, *40*, 1018–1034. [[CrossRef](#)]
55. Sakurai, Y. An overview of the Oyashio ecosystem. *Deep Sea Res. Part II Top. Stud. Oceanogr.* **2007**, *54*, 2526–2542. [[CrossRef](#)]
56. Kaneko, H.; Tanaka, T.; Abe, H.; Wakita, M.; Sasaki, K.; Miyazawa, Y.; Okunishi, T.; Watanabe, S.; Tatamisashi, S.; Sato, Y. Subinertial frequency variations in the axis of the Tsugaru Warm Current east of the Tsugaru Strait. *Prog. Earth Planet. Sci.* **2022**, *9*, 53. [[CrossRef](#)]
57. Uchimoto, K.; Mitsudera, H.; Ebuchi, N.; Miyazawa, Y. Anticyclonic eddy caused by the Soya Warm Current in an Okhotsk OGCM. *J. Oceanogr.* **2007**, *63*, 379–391. [[CrossRef](#)]
58. Appen, W.-J.; Wekerle, C.; Hehemann, L.; Schourup-Kristensen, V.; Konrad, C.; Iversen, M.H. Observations of a Submesoscale Cyclonic Filament in the Marginal Ice Zone. *Geophys. Res. Lett.* **2018**, *45*, 6141–6149. [[CrossRef](#)]
59. Kozlov, I.E.; Atadzhanova, O.A. Eddies in the Marginal Ice Zone of Fram Strait and Svalbard from Spaceborne SAR Observations in Winter. *Remote Sens.* **2022**, *14*, 134. [[CrossRef](#)]
60. Srinivasan, K.; McWilliams, J.C.; Molemaker, M.J.; Barkan, R. Submesoscale Vortical Wakes in the Lee of Topography. *J. Phys. Oceanogr.* **2019**, *49*, 1949–1971. [[CrossRef](#)]
61. Cigna, F.; Tapete, D. Present-day land subsidence rates, surface faulting hazard and risk in Mexico City with 2014–2020 Sentinel-1 IW InSAR. *Remote Sens. Environ.* **2021**, *253*, 112161. [[CrossRef](#)]

62. Yagüe-Martínez, N.; Prats-Iraola, P.; González, F.R.; Bricic, R.; Shau, R.; Geudtner, D.; Eineder, M.; Bamler, R. Interferometric Processing of Sentinel-1 TOPS Data. *IEEE Trans. Geosci. Remote Sens.* **2016**, *54*, 2220–2234. [[CrossRef](#)]
63. Lavrova, O.; Serebryany, A.; Bocharova, T.; Mityagina, M. Investigation of fine spatial structure of currents and submesoscale eddies based on satellite radar data and concurrent acoustic measurements. In *Remote Sensing of the Ocean, Sea Ice, Coastal Waters, and Large Water Regions 2012*; SPIE: Edinburgh, UK, 2012; pp. 155–168. [[CrossRef](#)]
64. Filipponi, F. Sentinel-1 GRD Preprocessing Workflow. *Proceedings* **2019**, *18*, 11. [[CrossRef](#)]
65. Zuiderveld, K. Contrast limited adaptive histogram equalization. *Graph. Gems* **1994**, *IV*, 474–485.
66. Xu, J.; Pan, X.; Jia, B.; Wu, X.; Liu, P.; Li, B. Oil Spill Detection Using LBP Feature and K-Means Clustering in Shipborne Radar Image. *J. Mar. Sci. Eng.* **2021**, *9*, 65. [[CrossRef](#)]
67. Stuhlmacher, A.; Gade, M. Statistical analyses of eddies in the Western Mediterranean Sea based on Synthetic Aperture Radar imagery. *Remote Sens. Environ.* **2020**, *250*, 112023. [[CrossRef](#)]
68. Dong, C.; McWilliams, J.C.; Shchepetkin, A.F. Island Wakes in Deep Water. *J. Phys. Oceanogr.* **2007**, *37*, 962–981. [[CrossRef](#)]
69. Zheng, Q. *Satellite SAR Detection of Sub-Mesoscale Ocean Dynamic Processes*; World Scientific: Singapore, 2017; Volume 44.
70. Shcherbina, A.Y.; D’Asaro, E.A.; Lee, C.M.; Klymak, J.M.; Molemaker, M.J.; McWilliams, J.C. Statistics of vertical vorticity, divergence, and strain in a developed submesoscale turbulence field. *Geophys. Res. Lett.* **2013**, *40*, 4706–4711. [[CrossRef](#)]
71. Brannigan, L.; Marshall, D.P.; Naveira Garabato, A.C.; Nurser, A.J.G.; Kaiser, J. Submesoscale Instabilities in Mesoscale Eddies. *J. Phys. Oceanogr.* **2017**, *47*, 3061–3085. [[CrossRef](#)]
72. Manucharyan, G.E.; Thompson, A.F. Submesoscale Sea Ice–Ocean Interactions in Marginal Ice Zones. *J. Geophys. Res. Ocean.* **2017**, *122*, 9455–9475. [[CrossRef](#)]
73. Elkin, D.N.; Zatsepin, A.G. Laboratory study of a shear instability of an alongshore sea current. *Oceanology* **2014**, *54*, 576–582. [[CrossRef](#)]
74. Callendar, W.; Klymak, J.M.; Foreman, M.G.G. Tidal generation of large sub-mesoscale eddy dipoles. *Ocean. Sci.* **2011**, *7*, 487–502. [[CrossRef](#)]
75. McWilliams, J.C. Submesoscale currents in the ocean. *Proc. R. Soc. A Math. Phys. Eng. Sci.* **2016**, *472*, 32. [[CrossRef](#)] [[PubMed](#)]
76. Thompson, A.F.; Lazar, A.; Buckingham, C.; Naveira Garabato, A.C.; Damerell, G.M.; Heywood, K.J. Open-Ocean Submesoscale Motions: A Full Seasonal Cycle of Mixed Layer Instabilities from Gliders. *J. Phys. Oceanogr.* **2016**, *46*, 1285–1307. [[CrossRef](#)]
77. Cao, Y.; Dong, C.; Qiu, Z.; Bethel, B.J.; Shi, H.; Lü, H.; Cheng, Y. Corrections of Mesoscale Eddies and Kuroshio Extension Surface Velocities Derived from Satellite Altimeters. *Remote Sens.* **2023**, *15*, 184. [[CrossRef](#)]
78. Liu, F.; Liu, Y.; Tang, S.; Li, Q. Oceanic Kármán Vortex Streets in the Luzon Strait in the Lee of Didicas Island from Multiple Satellite Missions. *Remote Sens.* **2022**, *14*, 4136. [[CrossRef](#)]
79. Tomczak, M. Island wakes in deep and shallow water. *J. Geophys. Res. Ocean.* **1988**, *93*, 5153–5154. [[CrossRef](#)]
80. Ni, Q.; Zhai, X.; Wilson, C.; Chen, C.; Chen, D. Submesoscale Eddies in the South China Sea. *Geophys. Res. Lett.* **2021**, *48*, e2020GL091555. [[CrossRef](#)]
81. Zhang, Y.; Hu, C.; Liu, Y.; Weisberg, R.H.; Kourafalou, V.H. Submesoscale and Mesoscale Eddies in the Florida Straits: Observations from Satellite Ocean Color Measurements. *Geophys. Res. Lett.* **2019**, *46*, 13262–13270. [[CrossRef](#)]

Disclaimer/Publisher’s Note: The statements, opinions and data contained in all publications are solely those of the individual author(s) and contributor(s) and not of MDPI and/or the editor(s). MDPI and/or the editor(s) disclaim responsibility for any injury to people or property resulting from any ideas, methods, instructions or products referred to in the content.